Int J Appl Earth Obs Geoinformation 90 (2020) 102119

Contents lists available at ScienceDirect

Int J Appl Earth Obs Geoinformation

journal homepage: www.elsevier.com/locate/jag

The 2019 Brumadinho tailings dam collapse: Possible cause and impacts of the worst human and environmental disaster in Brazil

Luiz Henrique Silva Rotta[a,*], Enner Alcântara[b], Edward Park[c], Rogério Galante Negri[b], Yunung Nina Lin[d], Nariane Bernardo[a], Tatiana Sussel Gonçalves Mendes[b], Carlos Roberto Souza Filho[e]

[a] São Paulo State University – Unesp, Department of Cartography, Brazil
[b] São Paulo State University – Unesp, Department of Environmental Engineering, Brazil
[c] National Institute of Education and Asian School of the Environment, Nanyang Technological University, Singapore
[d] Institute of Earth Sciences, Academia Sinica, Taiwan
[e] University of Campinas – Unicamp, Institute of Geosciences, Brazil

ARTICLE INFO

Keywords:
Dam collapse
Mining
Contaminated mud
Suspended particulate matter
Remote sensing

ABSTRACT

On 25th January 2019, the tailings dam of the Brumadinho iron mine operated by Vale S/A failed catastrophically. The death toll stood at 259 and 11 people remained missing as of January 2020. This tragedy occurred three years after Mariana's tailings dam rupture – the most significant tailing dam disaster in Brazilian history. Thus far, a systematic investigation on the cause and effect of the failure has yet to be conducted. Here, we use satellite-driven soil moisture index, multispectral high-resolution imagery and Interferometric Synthetic Aperture Radar (InSAR) products to assess pre-disaster scenarios and the direct causes of the tailings dam collapse. A decreasing trend in the moisture content at the surface and the full evanescence of pond water through time (2011–2019) suggest that the water was gradually penetrating the fill downwards and caused the seepage erosion, saturating the tailings dam. Large-scale slumping of the dam (extensional failure) upon the rupture indicates that the materials of the fill were already saturated. InSAR measurements reveal a dramatic, up to 30 cm subsidence in the dam (at the rear part) within the past 12 months before the dam collapse, signifying that the sediments had been removed from the fill. Although the information on the resistance level of the tailings dam to infiltrations is not available, these pieces of evidence collectively indicate that the seepage erosion (piping) is the primary cause for the chronic weakening of the structure and, hence, the internal "liquefaction" condition. Upon the collapse, the fully saturated mud tailings flowed down the gentle slope area (3.13×10^6 m^2), where 73 % were originally covered by tree, grass or agricultural tracts. The toxic mud eventually reached the Paraopeba River after travelling 10 km, abruptly increasing the suspended particulate matter (SPM) concentration and the toxic chemical elements in the river, immediately affecting the local livelihoods that depend on its water. The Paraopeba River is a major tributary of the San Francisco River, the second-longest river in Brazil reaching the Atlantic Ocean. We anticipate that the environmental repercussions of this toxic seepage will be felt throughout the entire basin, especially riverine communities located downstream.

1. Introduction

A Brazilian mining disaster, also known as the Samarco disaster, occurred on 5th November 2015 at the Fundão dam located around Mariana city, Minas Gerais State. The mud wave produced by the dam failure, estimated at 43 million m^3, spread over several kilometers down the slope, reaching the the Doce River, the second-longest river in Brazil (Garcia et al., 2007), turning it into a "sea" of red mud (Hatje et al., 2017). This river served as a primary source of water and fish for several local communities.Subsequently, the contaminants in the Doce River were delivered to the Atlantic Ocean, after travelling around 665 km (Aires et al., 2018), seriously affecting coastal environments and marine ecosystems (Carmo et al., 2017; Coimbra et al., 2019). Besides the extensive and serious water pollution, the disaster also killed 20 people, caused mass death of fishes, flooded almost 7000 km^2 that covered the Bento Rodrigues district, and adversely affected the Abrolhos Marine National Park (Francini-Filho et al., 2019). Economic losses were estimated at around US$ 521 million per year (Garcia et al.,

* Corresponding author at: São Paulo State University, Department of Cartography, 19060-900, Roberto Simonsen 305, Presidente Prudente, SP, Brazil.
E-mail address: lh.rotta@unesp.br (L.H. Silva Rotta).

https://doi.org/10.1016/j.jag.2020.102119
Received 8 January 2020; Received in revised form 26 March 2020; Accepted 26 March 2020

2007), and rigorous and vigilant protocols were proposed to assess other dams in a similar condition in the country aiming to prevent history from repeating.

After 3 years of the Mariana tragedy, on 25th January 2019, another mining dam consisting of iron ore tailings failed catastrophically in the Brumadinho city, Minas Gerais State, Brazil. The rupture produced more than 11×10^6 m^3 of mining waste – equivalent to a 10-m high wave of mud that spread 10 km the downhill – that reached the Paraopeba River; a major tributary of the São Francisco River. Although the volume of mud derived from the Brumadinho disaster is less than the case of Mariana, the event caused far more significant loss of lives. As of January 2020, the death toll hit 259 people, while 11 individuals remain missing.

Both collapsed dams belong to Vale S/A, which owns 133 iron ore dams in Brazil, of which 80 % of them (105) are in the Minas Gerais State. Vale uses both downstream (conventional model) and upstream tailings dams. The upstream tailing dam, the model used both in Brumadinho and Mariana, is constructed by vertically accumulating the tailings through successive uphill deposition (Kossoff et al., 2014**)**. This dam filling method is cheaper since only moderate compaction of a smaller amount of material is required. The license for such dam projects are also easily obtained since upstream tailing dams occupies a smaller area relative to the downstream tailing dams. This upstream tailing dam model, however, is considered dangerous and risky (Kossoff et al., 2014), becausethe stability of the tailings impoundments decreases substantially once operations cease (Martin and McRoberts, 1999). Generally, the disposal management in such a dam aims to form a uniform deposit, whereby the coarser solids are deposited adjacent to the embankment. A supernatant pond is formed by managing the beach to ensure the run-off, enabling decanting and re-use. The dam stability, therefore, relies on the earthfill/tailings strength (used to construct each bund), the characteristics of the tailings and the maintenance of the tailings pond at a safer distance from the structure zone (Cambridge and Shaw, 2019). Since 2015, when the Brumadinho dam was deactivated, it received several positive assessments by the local consultants on dam safety and seepage/stability (Porsani et al., 2019). However, despite systematic monitoring, it failed three years after closure, conflicting with the notion that geotechnical structures become more stable over time (Santamarina et al., 2019).

Here, we investigate possible causes of the dam failure and discuss the environmental consequences of the tragedy. We attempt to understand the changes in moisture contents at the surface of the Brumadinho tailings dam and hypothesize that the seepage erosion followed by the liquefaction and gradual removal of the fill have led to the failure of the dam. The main environmental impacts caused by the mudflow were also investigated using available remote sensing data. Specifically, we aim (i) to investigate the possible cause of the dam rupture using various available remote sensing datasets, (ii) to map the impact of mudflows on land use and land cover changes (LULCC), (iii) to compare the suspended particulate matter (SPM) in the Paraopeba River before and after the dam rupture, and (iv) to assess the geochemical impact on the Paraopeba River.

2. Site description

The complex of iron dams is located at upstream of the Brumadinho city in Minas Gerais State, southeastern Brazil (Fig. 1a). The watershed of the Paraopeba River (WPR) is located at the center of Minas Gerais State, with the area of 13,640 km^2, draining directly into Três Marias hydroelectric reservoir (Durães et al., 2016). The Paraopeba River has large-scale sand-extraction industrial operations and is located near highly populated areas with extensive iron mining activities (Sato and Godinho, 2003). Fig. 1 shows the location of the collapsed dam, as well as high-resolution images acquired by Planet constellation satellites before and after the dam rupture.

An image acquired on January 29th 2019, shows the area directly affected by the mudflow (Fig. 1). The mud traveled approximately 10 km, reaching the Paraopeba River. The mud covered an area of 3.13×10^6 m^2, equivalent to 450 football fields. The collapsed dam (Dam I - Córrego do Feijão Mine) had an area of 4.13×10^5 m^2 and approximately 600 m width.

3. Methods

3.1. Soil Moisture Index (SMI)

The Soil Moisture Index (SMI) over the tailings dam (Lambin and Ehrlich, 1996; Zhan et al., 2004) was used to reconstruct the dynamics of the ponding over the dam since 2011. This information is important in assessing the cause of the failure because the dam was decommissioned in 2015. Therefore, the pond over the dam is expected to disappear over time. Landsat 5, 7 and 8 images between 2011 and 2019 were used to calculate the SMI. This index is based on the Normalized Difference Vegetation Index (NDVI) and Land Surface Temperature (LST), yielding values between 0 (drier soil) and 1 (wet soil), which is calculated as (Zhan et al., 2004):

$$SMI = \frac{LST_{max} - LST}{LST_{max} - LST_{min}} \quad (1)$$

where, LST_{max} and LST_{min} are, respectively, the maximum and minimum values of LST within the image for a given NDVI, expressed as:

$$LST_{max} = a_1 \times NDVI + b_1 \quad (2)$$

$$LST_{min} = a_2 \times NDVI + b_2 \quad (3)$$

where, a and b are empirical parameters defining the dry and wet edges modeled as a linear fit to the data (Zhan et al., 2004; Parida et al., 2008; Potić et al., 2017).

According to Lambin and Ehrlich (1996), the scatterplot of LST vs NDVI results in a trapezoidal shape, and all types of land cover fall within the trapezoid of the LST-NDVI space. The upper envelope of the trapezoid (upper limit of surface temperature for a given vegetation cover) represents the dry condition (warm edge), while the lower limit represents the wet condition (cold edge) (Parida et al., 2008).

A time series of SMIs was retrieved from TM/Landsat-5, ETM +/Landsat-7 and OLI/Landsat-8 images (Table 1). The images used are surface reflectance products (L3) at 30 m resolution, which were downloaded from the USGS Earth Explorer site (https://earthexplorer.usgs.gov).

We generated a standard deviation map of SMI over time to analyze the variation of moisture conditions over the dam. Upon the dam rupture, the mud flowed into the Paraopeba River, dramatically affecting the water quality. Remote sensing images were also used to compare the SPM concentrations before and after the rupture.

3.2. Interferometric synthetic aperture radar

We obtained 33 scenes from Sentinel-1 Synthetic Aperture Radar (SAR) descending path 53 between Jan 3rd 2018 and Jan 22nd 2019. Given the regular acquisition frequency of every 12 days, we adopted the nearest-2 paring strategy to produce 63 SAR interferograms. The processing was done using NASA JPL's opensource software ISCE2 (https://github.com/isce-framework/isce2). All interferograms are geocoded at 15×15 m ground pixel spacing using an oversampled SRTMv3 DEM (Farr et al., 2007) by a factor of two. To compute the surface line-of-sight (LOS) displacement time-series from the pairwise interferograms, we choose the small baseline subset approach (Berardino et al., 2002) in the Generic InSAR Analysis Toolbox (GIAnT; Agram et al., 2013). We incorporated simple tropospheric correction by removing the topographically-correlated phase (Lin et al., 2010). The standard deviation of the LOS displacement time-series was derived

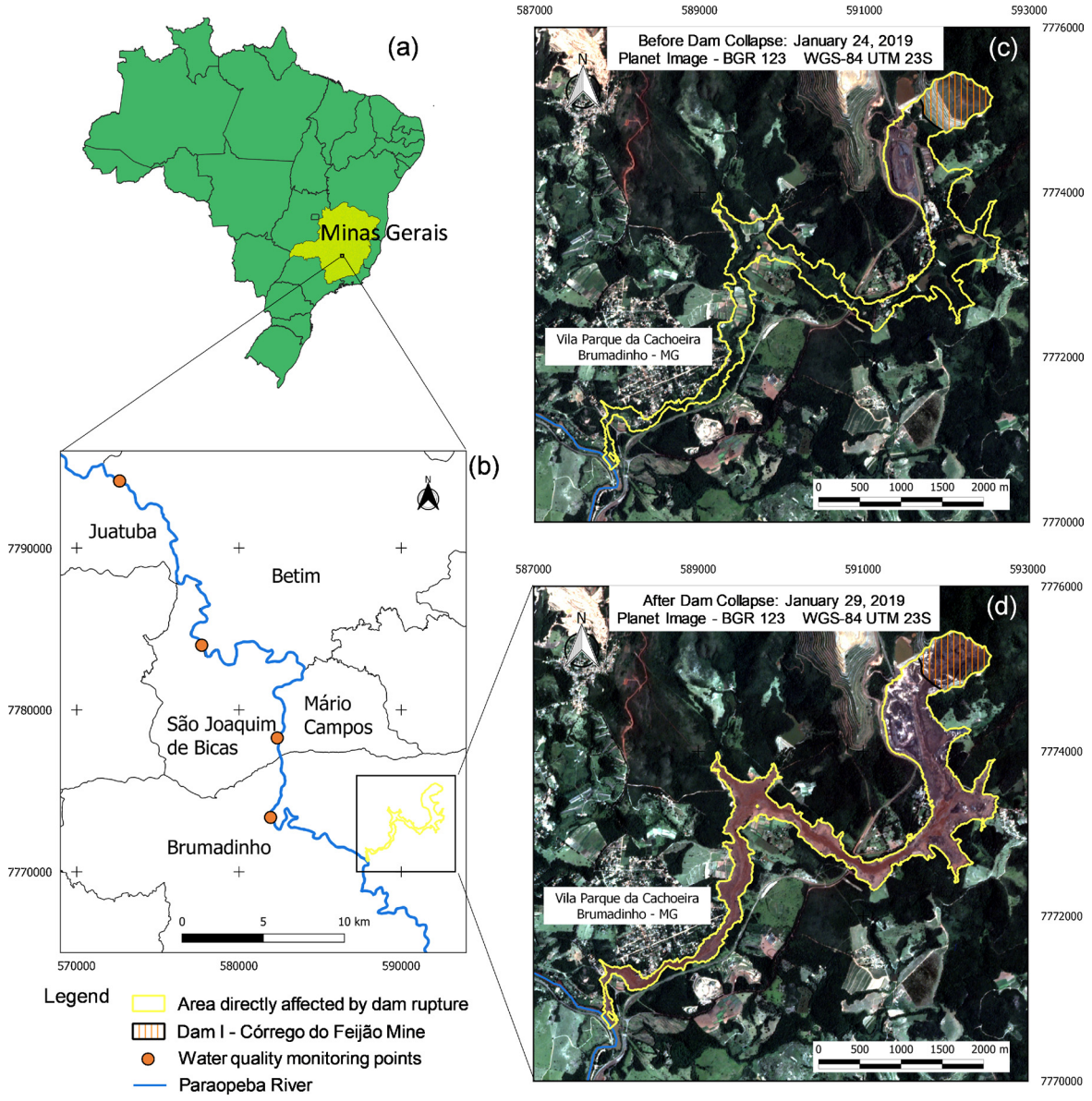

Fig. 1. Study area: (a) Minas Gerais State in Brazil; (b) Paraopeba River and cities near to the accident; (c) before and (d) after images of the dam collapse, indicating the dam location and the area directly affected by the mud wave.

Table 1
Summary of the TM/Landsat-5, ETM+/Landsat 7 and OLI/Landsat 8 images used in this study.

Date	Sensor	Date	Sensor	Date	Sensor
2011-02-09	TM L5	2013-10-28	OLI L8	2016-07-16	OLI L8
2011-04-14	TM L5	2014-04-06	OLI L8	2016-08-17	OLI L8
2011-04-30	TM L5	2014-05-24	OLI L8	2016-09-18	OLI L8
2011-06-17	TM L5	2014-06-09	OLI L8	2016-12-07	OLI L8
2011-07-19	TM L5	2014-08-12	OLI L8	2016-12-23	OLI L8
2011-08-04	TM L5	2014-09-29	OLI L8	2017-01-08	OLI L8
2011-09-05	TM L5	2014-11-16	OLI L8	2017-03-13	OLI L8
2011-09-21	TM L5	2015-01-03	OLI L8	2017-07-03	OLI L8
2011-10-07	TM L5	2015-05-27	OLI L8	2017-09-05	OLI L8
2012-09-15	ETM + L7	2015-06-12	OLI L8	2017-10-07	OLI L8
2013-02-22	ETM + L7	2015-07-30	OLI L8	2018-04-17	OLI L8
2013-04-27	ETM + L7	2015-08-31	OLI L8	2018-05-03	OLI L8
2013-07-16	ETM + L7	2015-09-16	OLI L8	2018-06-04	OLI L8
2013-08-01	ETM + L7	2015-10-02	OLI L8	2018-07-06	OLI L8
2013-11-21	ETM + L7	2016-03-10	OLI L8	2018-09-08	OLI L8
2013-07-08	OLI L8	2016-04-11	OLI L8	2018-12-13	OLI L8
2013-08-25	OLI L8	2016-06-14	OLI L8	2019-01-14	OLI L8

through a regular bootstrapping approach.

3.3. Land use and land cover mapping

We delineated the affected area by using Planet images acquired before (January 22nd, 2019) and after (January 27th 2019) the dam rupture (Fig. 1). The Planet constellation consists of more than 130 orbital Earth observation satellites acquiring daily images of the Earth on four bands in the visible and near infrared wavelength range at 3 m spatial resolution (www.planet.com). The affected area was automatically vectorized by differencing the Normalized Difference Vegetation Index (NDVI) from images before and after the dam collapse. Using the NDVI difference image, the area with more significant land cover changes was easily identified, which is the area covered by the mud tailings (Fig. 1d).

We mapped the Land Use and Land Cover Changes (LULCC) of the area using a Support Vector Machine (SVM) algorithm (Mountrakis et al., 2011). The Planet image acquired on January 22nd 2019 (before the collapse) was selected for the classification. The SVM approach yields robust results whilst requiring limited training data. It also has a

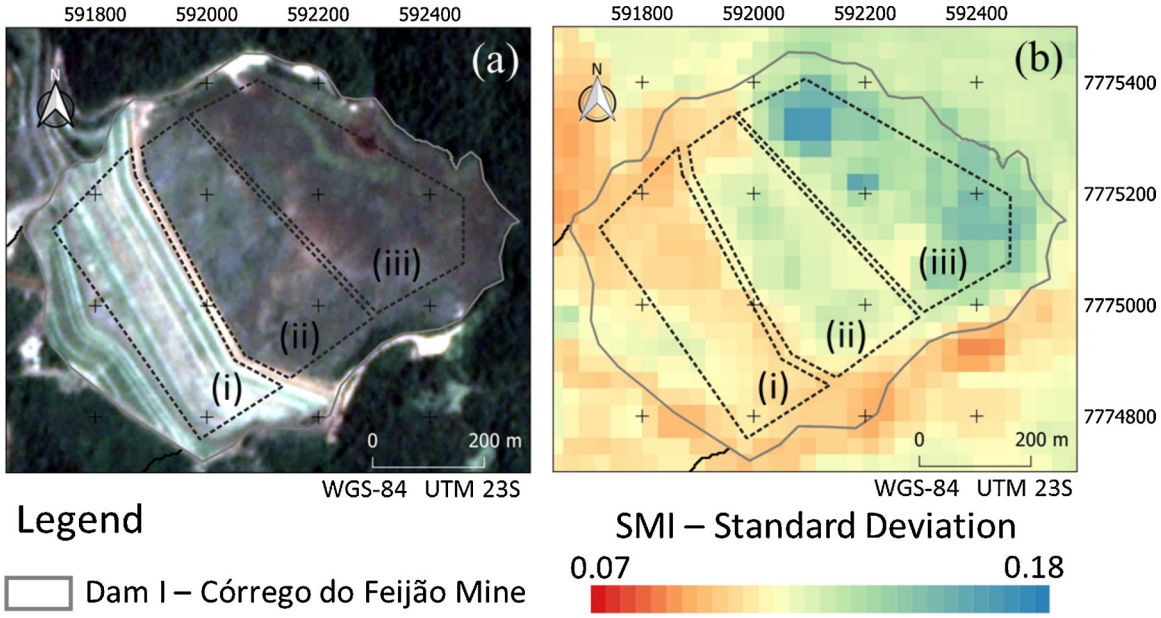

Fig. 2. Planet satellite image form 24 January 2019 (a) and SMI Standard Deviation map from 2011 to 2019 of the Dam I – Córrego do Feijão Mine (b). Three specific sectors of the dam are considered for analysis: Slope (i), Top-of-bench-1 (ii) and Top-of-bench-2 (iii).

high generalization capability in comparison to other conventional classification methods (Mountrakis et al., 2011).

Classes of "tree vegetation", "grass/agriculture", "water body" and "bare soil" were considered and respective training and test samples were collected through visual inspection of the images. To evaluate the classification results, a confusion matrix between the classified image and the ground truth data was generated to calculate the Kappa coefficient. Regions of interest (ROIs) of the four classes were created and used in classification and validation. The "building" class was created manually because of the high confusion among the other classes. Furthermore, the "Dam I – Córrego do Feijão Mine" class was inserted in the LULCC map to identify its location in the area affected by the mud tailings. The SVM parameters were empirically tuned, yielding a penalty value of 100 and RBF kernel function with gamma parameter of 0.25. Furthermore, the one-against-all multiclass strategy was employed.

In addition to the LULCC mapping, we calculated slope and terrain roughness index (TRI) (Riley et al., 1999) of the impacted area using the SRTM DEM (30 m). TRI is defined as the mean difference between a central pixel and its eight surrounding cells.

3.4. Suspended Particulate Matter (SPM) mapping

We used Sentinel 2A images acquired by the Multispectral Instrument (MSI/Sentinel-2) to estimate the Suspended Particulate Matter (SPM) over the Paraopeba River. With a 10 m resolution at visible and near infrared bands, and 12-bit radiometric resolution, the MSI image is suitable to study small-scale inland water, i.e. water bodies with a diameter less than 30 m (Toming et al., 2016). Level 2A images (i.e., bottom-of-atmosphere corrected reflectance product) were downloaded from the Sentinel's Scientific Data Hub (http://scihub.copernicus.eu/) (tile 23KNT in Sentinel-2 mission system). The first image, acquired on January 22nd 2019, was used to estimate the water quality of the river before the dam failure. The second image, acquired on February 2nd 2019 (after the dam collapse), was used to assess the impact of the mudflows into the Paraopeba River.

The images were processed in SNAP (Sentinel Application Platform, https://step.esa.int/main/toolboxes/snap/), applying the semi-analytical SPM model from Nechad et al. (2010) (Eq. (4)). We used the near-infrared band (B8 - 845 nm) since the red band located at 665 nm was not sensitive enough to map the high level of SPM concentrations in the Paraopeba River after the dam collapse. The SPM concentration retrieval model used here is calculated by the following equation:

$$\mathrm{SPM} = \frac{A \times \rho_w}{1 - \frac{\rho_w}{C}} + \mathrm{B} \quad (4)$$

where ρ_w is the water reflectance; c is established according to Nechad et al. (2010) and the central wavelength (865 nm = 0.2115); B denotes measurements errors in reflectance. The parameter A (mg/l) provides the relationship between SPM and reflectance. We used an A value of 289.29 mg/l, adapted from Nechad et al. (2010).

The SPM was calculated along 60 km in the Paraopeba River downstream from the initial point of pollution in the water body, i.e. from Brumadinho to Juatuba (Fig. 1b). The Paraopeba River was divided into twelve regions (5 km each) to show the longitudinal distribution of SPM using a boxplot for each date. We also employed SPM median values to compare the pre- and post-collapse SPM conditions in the river.

4. Results and discussion

4.1. Moisture in the tailing dam

The SMI indicates the moisture in the study area and was calculated for 51 Landsat-5, 7 and 8 images between 2011 and 2019. The SMI standard deviation map is shown in Fig. 2.

Based on the SMI standard deviation map of the dam since 2011, different spatial variation patterns are highlighted that is used to divided the dam into three sections: (i) Slope sector, which hosts the downstream slope of the dam (face); (ii) Top-of-bench-1, which is the area closest to the slope; (iii) Top-of-bench-2, which is sector more distant from the slope that showed relatively higher SMI standard deviation within the dam. The observed higher moisture in the Top-of-bench-2 (iii) was also highlighted by Robertson et al. (2020); these authors showed that the water accumulation near the dam crest allows the deposition of weak tailings near the dam crest.

The SMI for twenty images from February 9th 2011 to January 14th 2019 is presented in Fig. 3.

Large tracts with a higher level of moisture were observed in the rear part of the dam (Fig. 3(iii) - Top-of-bench-2) until 2016. At the

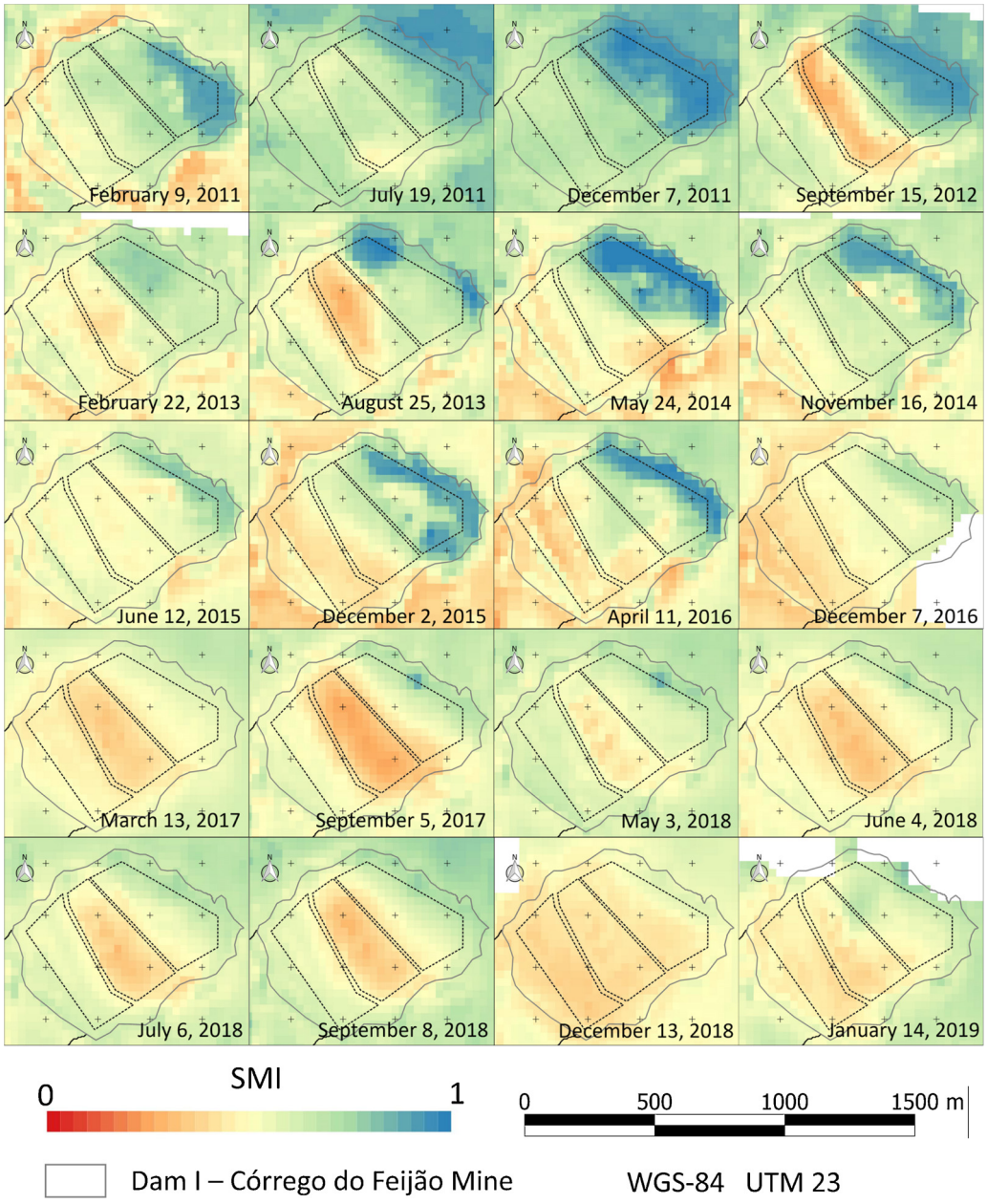

Fig. 3. Soil Moisture Index (SMI) from 2011 to 2019 based on sensors/satellites TM/Landsat-5, ETM+/Landsat7 and OLI/Landsat-8. The white patches represent areas in the images influenced by clouds (i.e., unusable data).

Top-of-bench-2 (iii), a significant water pond was then formed. The SMI for 5th September 2017; 3rd May 2018; 4th June 2018; and 8th September 2018 showed a smaller region with a higher moisture value (including a particular blue "bullseye" in the 5th September 2017 and 3rd May 2018 images), which may indicate a site with external water entry to the dam that might have contributed to increase the water content over the structure. The SMI in the dam by 14th January 2019 (11 days before the collapse of the Brumadinho dam) showed that Top-of-bench-2 (iii) was the sector with the highest moisture at that date, whereas Top-of-bench-1 (ii) and Slope (i) displayed similar SMI values. However, pixels with low SMI values were observed in Top-of-bench-1 (ii), near the transition between the slope and the flat top surface.

Fig. 4 shows the SMI for the sectors indicated in Fig. 2 (Slope (i), Top-of-bench-1 (ii) and Top-of-bench-2 (iii)) for all the images analyzed between 2011 and 2019. The images used to calculate SMI were evenly distributed through time, allowing an biased-free investigation of possible trends. Precipitation data acquired from the Tropical Rainfall Measuring Mission (TRMM) in Giovanni (giovanni.gsfc.nasa.gov) was plotted in the same diagram.

In general, higher SMI values were observed over the Top-of-bench-2 (iii) sector of the dam for the investigated period (Fig. 4). The observed high moisture contents might have implied that this sector was saturated with water. Another behavior observed is the decrease of SMI throughout the dam during the same period. Between 2011 and 2017, Slope (i) and Top-of-bench-1 (ii) showed similar behavior, with consistently lower values compared to Top-of-bench-2 (iii). After 2017, Slope (i) and Top-of-bench-2 (iii) presented similar SMI values. In the rainy season, comparable values were also noted in the three regions. However, in the dry period, the difference between Top-of-bench-1 (ii) and the other regions increases, i.e., the SMI of the Top-of-bench-1 (ii) decreased significantly in comparison to Top-of-bench-2 (iii) and Slope (i). We speculate that the increase in the moisture pattern between the top and the slope sectors, between 2017 and 2019 (i.e. after the dam was decommissioned in 2015), implied that the fill was becoming

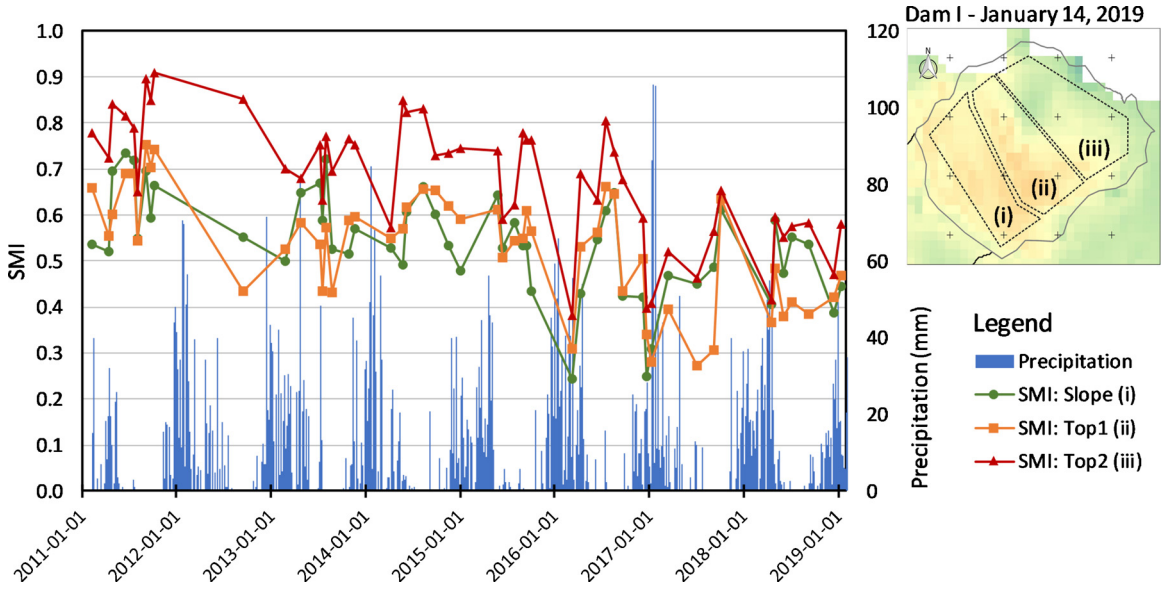

Fig. 4. SMI mean value between 2011 and 2019 for the sectors Slope(i), Top-of-bench-1(ii) and Top-of-bench-2(iii) in the Brumadinho tailings dam. Precipitation data from TRMM/Giovanni (giovanni.gsfc.nasa.gov).

water-saturated until it collapsed.

4.2. Deformation in the tailings dam

The sector of the dam with significant soil moisture had also sunk over the past few years (Top-of-bench-2, Fig. 4). We also observed the largest LOS displacement in the region, of up to −25 cm between January 2018 and January 2019 (point B in Fig. 5). As there are no concurrent ground-based displacement measurements available, there might remain a slight uncertainty in relation to the subsidence and westward motion, given the sensing direction of the descending path. However, since Top-of-bench-2 is topographically lower than Top-of-bench-1 according to the high-resolution ALOS2 DEM (Fig. 7c), we believe that westward motion is less likely and that the signal was likely to be causedby vertical subsidence. After accounting for the average incident angle of 32.5 degrees, the actual cumulative vertical displacement was estimated to be approximately -30 cm.

Besides the deformation within the tailings dam, we also observed creeping in the mountainous area abutting the dam (point A in Fig. 5) which began around August 2018 and continued up to the point the dam failed. This creeping might have been a result of on-going deformation within the dam and contributed to the final failure process.

4.3. Driving forces responsible for the dam failure

A time-lapse of high-resolution images over the tailings dam since 2011 (Fig. 6) revealed the dynamics of the drainage at the rear part of the dam, where ponds were formed (Top-of-bench-1 (ii)). These small drainages had gradually incised the surface and the ponds seemed to be the resultant depression from both the channel gullying and the gradual subsidence of the fill (as evidenced in Fig. 5). The accumulated water had gradually infiltrated through the fill, causing seepage erosion that led to the removal of material, which is often referred to as “piping”.

Both SMI time-series and the time-lapse high-resolution images suggest that despite the high precipitation in this area (Fig. 4), the volume of water in the pond gradually decreased throughout the years. Even if we assume that the precipitation was fully balanced by evapotranspiration and there was no net meteoric water gain (net loss is unlikely because the vegetation is dense there), it is estimated that there was still ~10,000 m^3 of water transferred out of the dam between

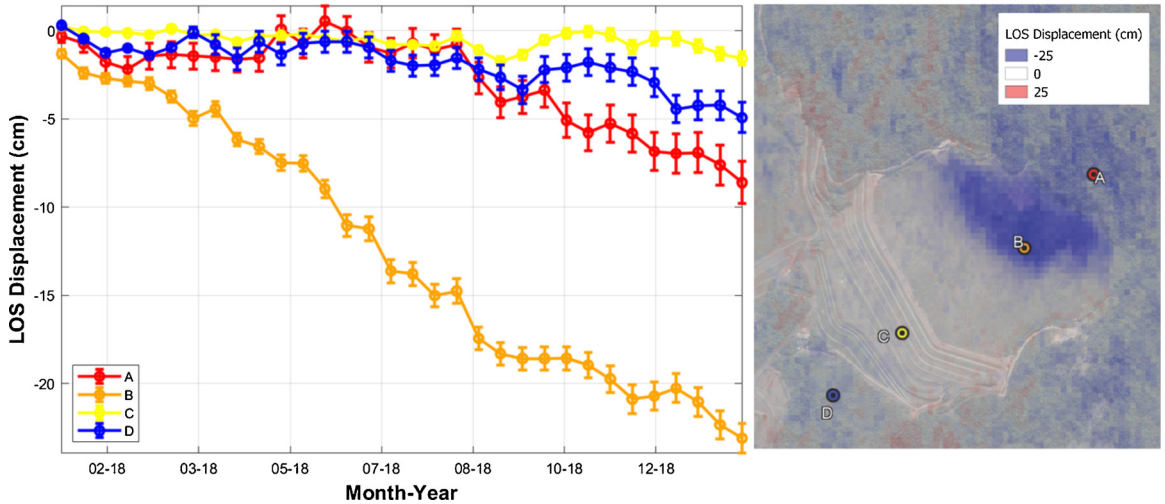

Fig. 5. Line-of-sight (LOS) displacement time-series from Sentinel-1 SAR interferograms. The LOS displacement map is for the total cumulated displacement between January 3rd 2018 and January 22nd 2019.

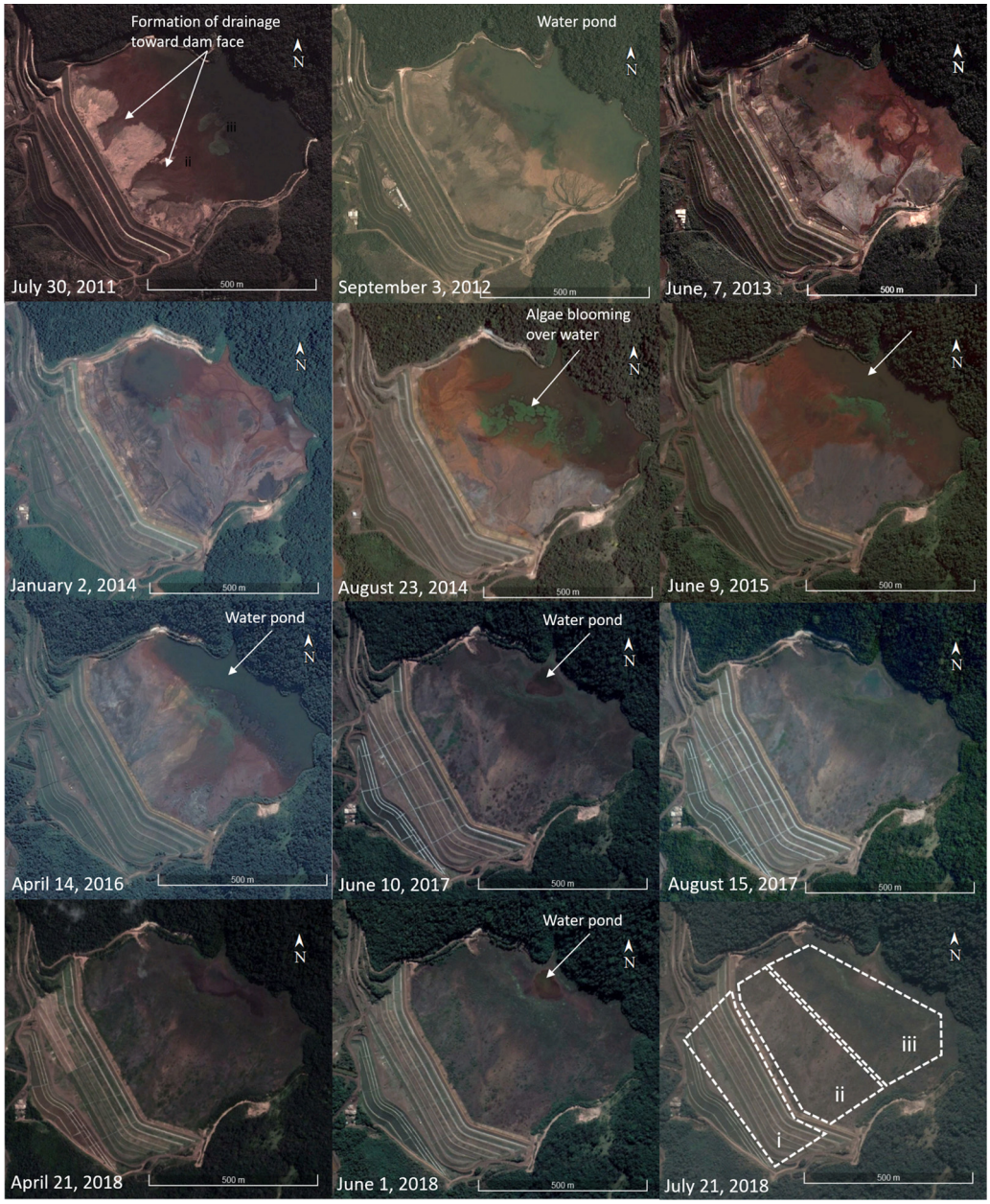

Fig. 6. Time-lapse of true-colour images, from Google Earth (2011-2018), showing the formation of drainage towards the dam slope and emplacement of ponds at the planar surface at the top of the fill. This indicates that the water table gradient was reaching the crest of the dam several years before the collapse. Algae blooms throughout the years also indicate that the stagnant condition of the pond has been persistent over time.

2011 and early 2018. Moreover, comparison of the InSAR displacement time-series with the optical images showed that displacement continued even after dried up completely around mid-July 2018 (Fig. 5). This high subsidence rate is even higher than that caused by groundwater pumping - a manmade, effective and directional process that usually reaches less than 10 cm/yr (e.g., see Ojha et al., 2018 and Riel et al., 2018 for studies in California).

Natural process like regular sediment compaction typically ranges between a few mm/yr (deltaic plains, Meckel et al., 2007) to a few cm/yr (reclaimed lands, Erten and Rossi, 2019; Sun et al., 2018). We, therefore, suggest that the mechanism to effectively remove water from the pond and materials from the fill is through fast seepage and seepage erosion (piping), which was the major cause of dam failure. The subsidence in the Top-of-bench-2 region resulted from the compaction of the void space, which happened after water was permanently removed from the pore space, together with potential material removal with the seepage. Upon the dam rupture, it initially seemed like that the failing started at the rear part of the surface (around Top 2(iii)), where the pond was formed close to the mountain area abutting the dam (point A in Figs. 5 and 7b). This failure through instantaneous “slumping” of the fill first happened in this area and was immediately followed by the weakening of the surrounding materials that were saturated with water (Fig. 7b).

The initial collapse at the rear part of the dam, where it experienced dramatic subsidence during 2018 (Fig. 5), triggered similar disturbances and large scale rotational slumping over the other parts of the fill. The mapping of the boundary of the slumping area through high-resolution photographs which were taken immediately before and after the collapse indicates that rotational slumping has occurred on the surface of the dam (Top-of-bench-1 (ii) and 2 (iii) zones) where the shear surface is circular (Fig. 7b, d and e). This implies that the water table was abnormally higher and perhaps reached close to the surface

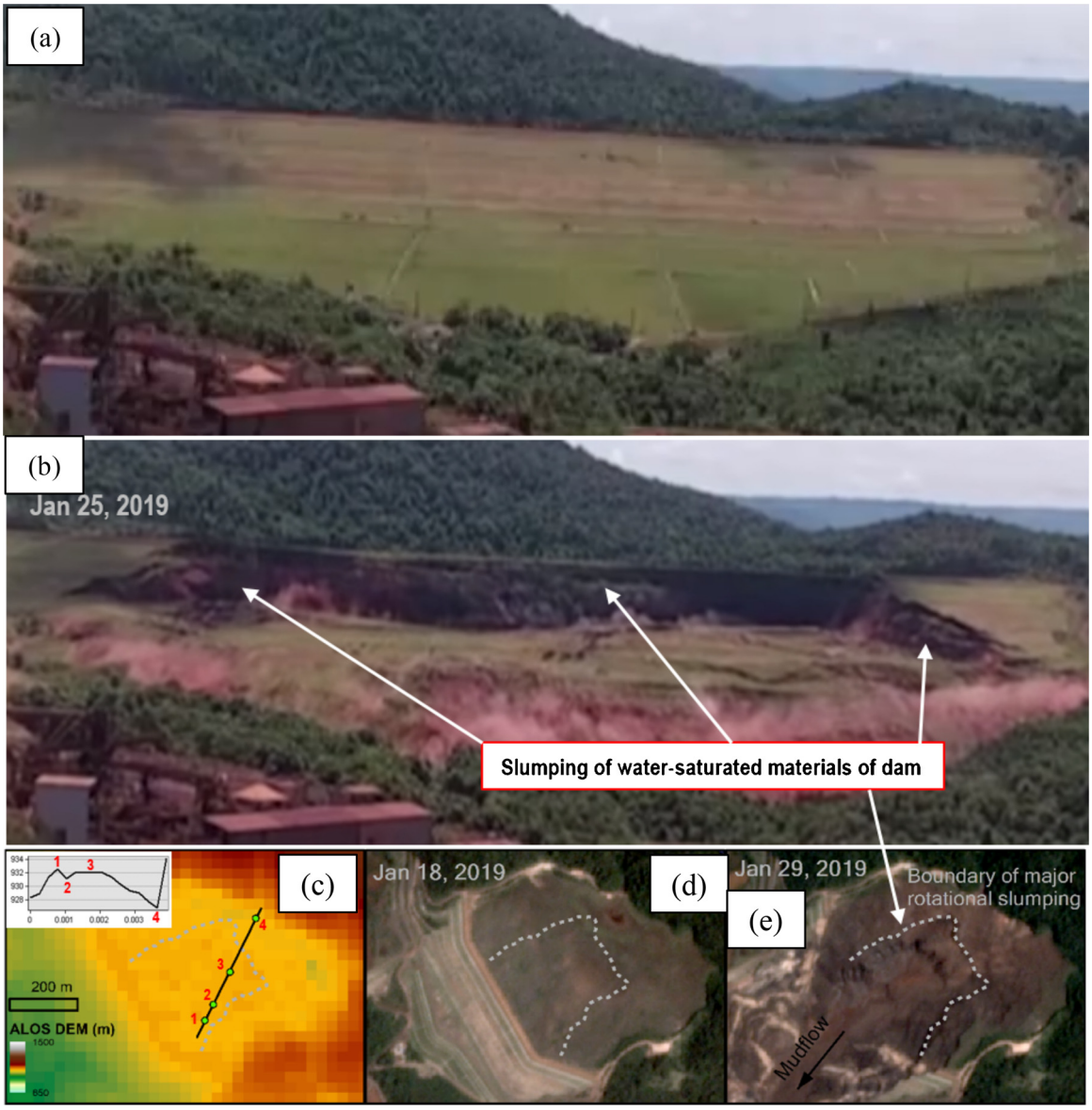

Fig. 7. (a) Screenshot from the movie (https://www.youtube.com/ watch?v = sKZUZQytads), immediately before the dam failure on January 25th, 2019. (b) Large scale slumping upon the dam failure. This indicates that the bulk of the fill was water-saturated before failure. (c) An elevation profile over the dam surface based on ALOS DEM acquired between 2008-2011. A depression with a depth around 4 m is shown towards the rear part of the fill, where the water pond is present during the wet seasons (Fig. 6). (d) and (e) High-resolution Planet images prior (Jan 18, 2019) and after the dam failure (Jan 29, 2019).

within both zones. Therefore, we consider that almost the entire dam was fully saturated when it failed, indicating that large scale "liquefaction" was already happening across the fill before it collapsed, as also indicated by the SMI mapping (Fig. 4).

According to Smith (2002), liquefaction is a phenomenon of deformation and collapse that could be caused by a triggering event and collapsible materials (e.g. tailings and water). Upon liquefaction, solid materials lose their mechanical resistance and present fluidal behavior (Morgenstern et al., 2016). In case of an earth-fill dam, liquefaction can also be triggered by constant rainfall or irrigations, through infiltration processes. After the collapse, the materials were flowing very fast (looks even as a turbulent flow) on a low gradient area (Fig. 8c, also evident from the video link in Fig. 7 caption), because they were in super-saturated condition, pushed downstream by high pore-pressure generated by the large scale slumping in the rear part of the dam.

Although we consider that water-saturated fill triggered the failure, more information – such as particle size distribution – which can only be obstained in the the field, is necessary to confirm the direct cause of the dam failure. Lack of sufficient compaction afterwards also should have increased the risk of failure.

4.4. Land use/cover in affected area by mud

The dam rupture directly impacted the ecosystem and human health mainly due to the toxic composition of the mud and the velocity of the mudflow that was released and engulfed habited areas, with no chances of survival during the event. Remote Sensing images provide historical records, such as pre- and post-disaster scenes. Mapping the differences between the two sets of images, usually carried through change detection techniques, helps the analysis of LULCC and, consequently offering information regarding the property's location and assessment of affected areas. The purpose of LULCC mapping in the mud-wave flooded areas extends beyond the identification of the changes, but also allows us to quantify environmental losses and impacts, as well as to provide support for management and planning actions. Fig. 8a shows the LULC map of the region before the dam failure, within the extent of

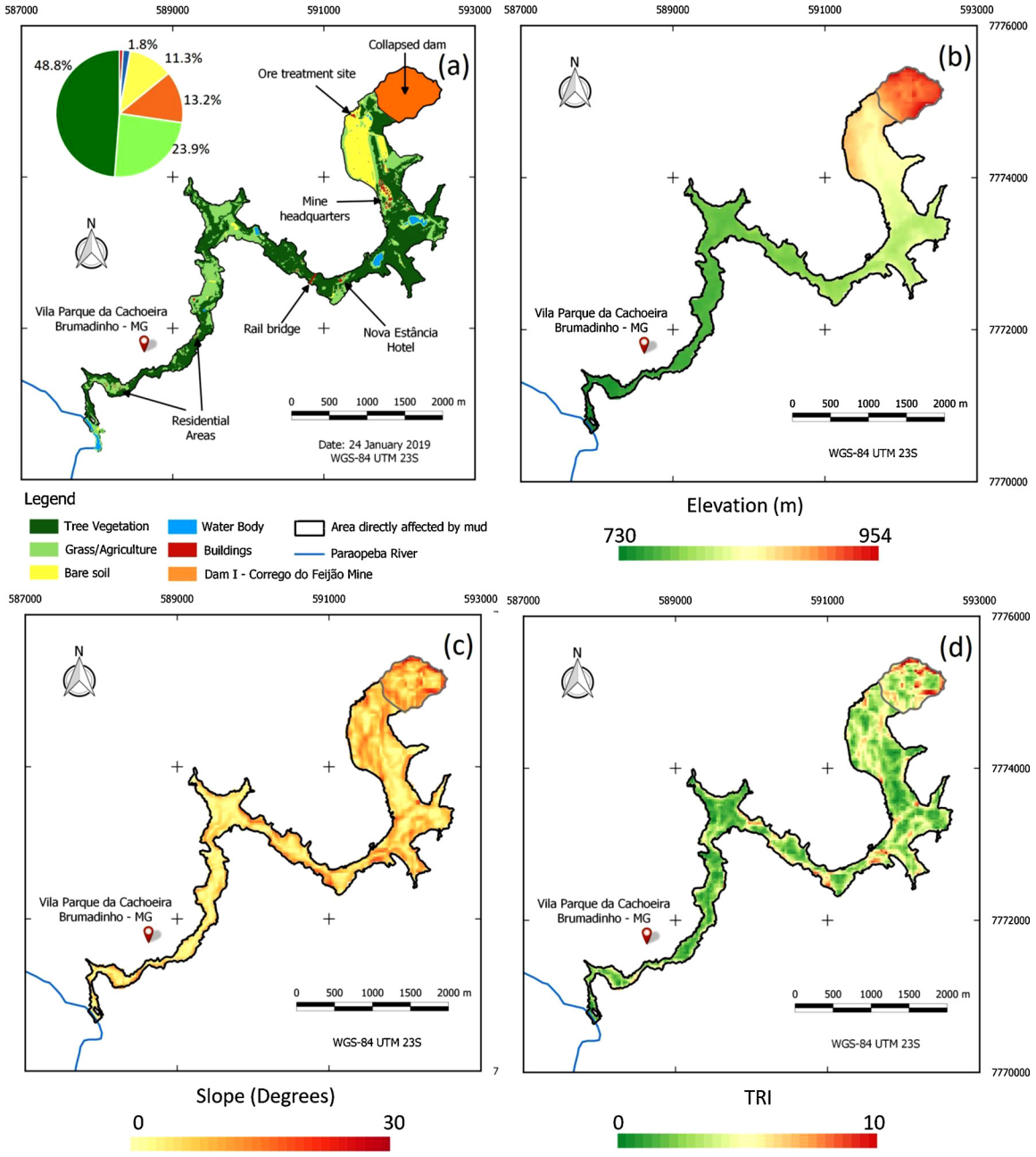

Fig. 8. The LULC map (a), Elevation (b), Slope (c) and Terrain Roughness Index (TRI) (d) of the area affected by the rupture of the tailings dam.

the mud-wave.

The class "Tree Vegetation" was the most affected by the mud, comprising 49 % of the analyzed area. This implies a huge loss of the ecosystem, with significant impacts on the local flora and fauna. About 24 % of the affected area comprised of regions with grass or agriculture. Agriculture is an important economic activity for people who live in the Vila Parque da Cachoeira. The regions classified as "Bare soil" (11 %) mostly result from mining activities. The tailings dam represents 13 % of the mapped area. The high difference in altitude between the tailings dam and the Paraopeba River (> 200 m as shown in Fig. 8b) and the moderate roughness of the terrain (Fig. 8d) accelerated the mud-flow. The affected area is mainly a mixture of Tree and Agriculture/Grass. Agricultural areas typically have low roughness and mostly occur on flat terrain, whereas trees usually have higher roughness and occupy predominantly steeper surfaces (Fig. 8a, c, and d). Therefore, the roughness of the terrain, depending on LULC, affected the rate at which mudflows reached the river.

The first targets hit by the mudflow were the mining workers located in ore treatment site and mine headquarters. The Nova Estancia hotel, which was operating during the disaster, had its employees and guests buried by the mud. The rail bridge was destroyed and washed away by the mudflow, showing the high stream power of the mud running downhill (Fig. 8a). Based on satellite images it is difficult to determine the exact number of buildings inside the area affected by the dam rupture. The industrial facilities at the ore extraction unit and the residential areas of Córrego do Feijão and Parque da Cachoeira districts were the main populated areas reached by the mudflow. The mud, full of toxics components, eventually reached the Paraopeba River, causing serious pollutions in the aquatic system (Thompson et al., 2020). The Paraopeba River is an important tributary of the São Francisco River – one of the largest rivers in Brazil. Immediately after the input of the tailings mud, the river's SPM concentration

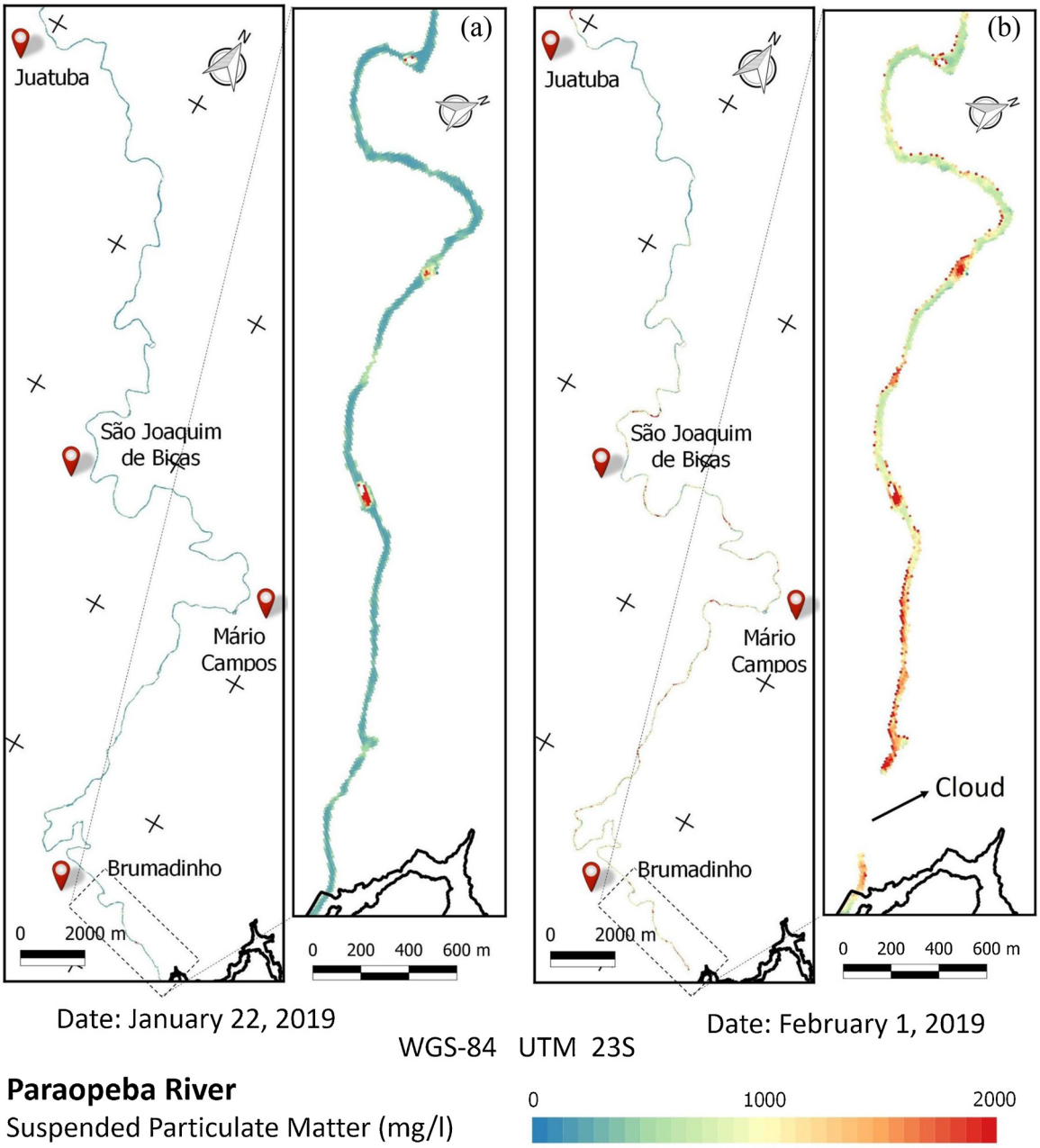

Fig. 9. Suspended particulate matter (SPM) from the affected area and up to 60 km along the Paraopeba River, before (a) (January 22nd, 2019) and after (b) (February 1st, 2019) the dam rupture.

increaseddramaticallyAccording to Souza (2019), the environmental impacts of Brumadinho dam rupture was massive and difficult to quantify.

4.5. SPM in the Paraopeba River

Fig. 9 shows the SPM concentration maps of the Paraopeba River before (January 22nd 2019) and after (February 1st 2019) the dam collapse. SPM boxplots are shown in Fig. 10. Using the median of the SPM concentrations of every 5 km along 60 km downstream, we found a remarkable difference between the two maps (Fig. 10). Although SPM values of up to 3000 mg/l are observed in the boxplot after the dam rupture, only a few points exceeded 2000 mg/l. Thus, to better visualize the difference in SPM concentrations, we used a palette ranging from 0 to 2,000 mg/l.

On January 22nd 2019, the SPM remained relatively constant throughout the first 60 km of the Paraopeba river (Fig. 9a), which is also shown in the boxplot (Fig. 10a). Mean values between 200 and 300 mg/l were observed in the river before the dam rupture. On February 1st 2019 (after the accident) the SPM values displayed high variability along the river and the mean concentration dramatically increased, overall indicating the direct impact of the tailings mud. The highest concentrations of SPM (median between 700 and 1000 mg/l) were observed over a distance of up to 40 km. There was a decrease in the SPM values after 40 km; however, SPM values were still higher than those before the dam rupture. We propose that this decrease in SPM values was primarily due to the sedimentation of the suspended solids in that tract, as the river width becomes wider and flow velocity decreased (i.e. due to increased width/depth ratio). An increase in the SPM values on the map of February 1st 2019 was noted at ~60 km from the entry point of mud into the river, close to Juatuba. This increase in SPM may have occurred due to resuspension of solids caused mainly by

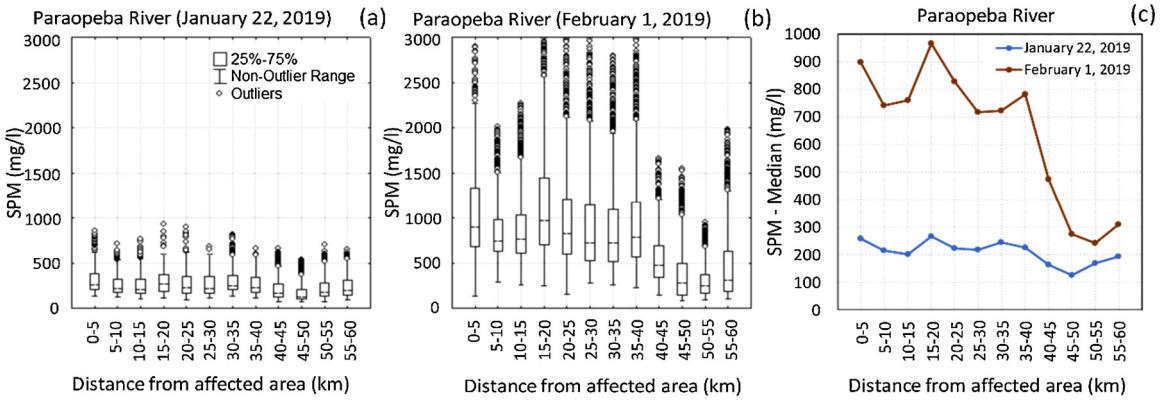

Fig. 10. SPM Boxplots from sections extracted at 5 km interval along the Paraopeba river before (January 22nd 2019) (a) and after (February 1st 2019) (b) the dam rupture. SPM median values are given in (c) for efficient comparison.

precipitation in that region, which has increased the turbulence locally.

5. Conclusion

In this paper, we investigated the possible cause of the impacts of the Brumadinho dam collapsed on the 25th January of 2019 in Brazil. The time series analysis of satellite-driven soil moisture index showed that the water accumulated over the Brumadinho dam surface during a protracted period increased its moisture contents and accelerated seepage erosion (piping) through the fill. We provide solid evidence of the seepage erosion from the top through the fill, which chronically weakened the structure and likely led to the collapse of the dam. The rapid subsidence rate measured by InSAR analysis (even after the pond dried out) and the large-scale slumping upon the rupture collectively indicates that the dam was undergoing the liquefaction process internally. The mudwave stemmed from the dam collapse killed more than 250 people and devastated huge forest and agricultural areas. The toxic mud reached the Paraopeba river after traveling ~10 km from the destruction site and the SPM concentration dramatically increased near the affected area reducing the light penetration into the water column, affecting the biological productivity.

CRediT authorship contribution statement

Luiz Henrique Silva Rotta: Conceptualization, Methodology, Formal analysis, Data curation, Writing - original draft. **Enner Alcântara:** Conceptualization, Methodology, Formal analysis, Writing - review & editing. **Edward Park:** Conceptualization, Methodology, Formal analysis, Writing - review & editing. **Rogério Galante Negri:** Formal analysis, Writing - review & editing. **Yunung Nina Lin:** Conceptualization, Methodology, Formal analysis, Writing - review & editing. **Nariane Bernardo:** Formal analysis, Writing - review & editing. **Tatiana Sussel Gonçalves Mendes:** Data curation, Writing - review & editing. **Carlos Roberto Souza Filho:** Conceptualization, Methodology, Writing - review & editing.

Declaration of Competing Interest

The authors declare that they have no known competing financial interests or personal relationships that could have appeared to influence the work reported in this paper.

Acknowledgements

E.A. acknowledge the Sao Paulo Research Foundation (FAPESP) under grant 19/00259-0. E.A. and C.R.S.F. acknowledge the Brazilian National Council for Scientific and Technological Development – CNPq for the research grants: 309712/2017-3 and 303169/2018-4, respectively. R.G.N. acknowledge FAPESP n° 2018/01033-3. L.H.S.R acknowledges the Coordination for the Improvement of Higher Education Personnel – (CAPES) for the postdoctoral fellowship. E.P. acknowledges the SUG-NAP (3/19EP) of the Nanyang Technological University. We acknowledge NASA for remote sensing data (Landsat and SRTM) used in this study.

References

Agram, P.S., Jolivet, R., Riel, B., Lin, Y.N., Simons, M., Hetland, E., Doin, M.P., Lasserre, C., 2013. New radar interferometric time series analysis toolbox released. Eos Trans. Am. Geophys. Union 94, 69–70.
Aires, U.R.V., et al., 2018. Changes in land use and land cover as a result of the failure of a miningtailings dam in Mariana, MG, Brazil. Land Use Policy 70, 63–70.
Berardino, P., Fornaro, G., Lanari, R., Sansosti, E., 2002. A new algorithm for surface deformation monitoring based on small baseline differential SAR interferograms. IEEE Trans. Geosci. Remote Sens. 40, 2375–2383.
Cambridge, M., Shaw, D., 2019. Preliminary reflections on the failure of the Brumadinho tailings dam in January 2019. Dams Reserv. 29, 113–123.
Carmo, F.F., et al., 2017. Fundão tailings dam failures: the environment tragedy of the largest technological disaster of Brazilian mining in global context. Perspect. Ecol. Conserv. 15, 145–151.
Coimbra, K.T.O., Alcântara, E.F.C., Souza Filho, C.R., 2019. An assessment of natural and manmade hazard effects on the underwater light field of the Rio Doce River continental shelf. Sci. Total Environ. 685, 1087–1096.
Durães, M.F., Mello, C.R., Beskow, S., 2016. Sediment yield in Paraopeba River Basin – MG, Brazil. Int. J. River Basin Manag. 14, 367–377.
Erten, E., Rossi, C., 2019. The worsening impacts of land reclamation assessed with Sentinel-1: the Rize (Turkey) test case. Int. J. Appl. Earth Obs. Geoinf. 74, 57–64.
Farr, T.G., et al., 2007. The shuttle radar topography mission. Rev. Geophys. 45, RG2004.
Francini-Filho, R.B., et al., 2019. Remote sensing, isotopic composition and metagenomics analyses revealed Doce River ore plume reached the southern Abrolhos Bank Reefs. Sci. Total Environ. 697, 132038.
Garcia, L.C., Ribeiro, D.B., Roque, F., de, O., Ochoa-Quintero, J.M., Laurance, W.F., 2007. Brazil's worst mining disaster: corporations must be compelled to pay the actual environmental costs. Ecol. Appl. 27, 5–9.
Hatje, V., et al., 2017. The environmental impacts of one of the largest tailing dam failures worldwide. Sci. Rep. 7, 1–13.
Kossoff, D., Dubbin, W.E., Alfredsson, M., Edwards, S.J., Macklin, M.G., Hudson-Edwards, K.A., 2014. Mine tailing dams: characteristics, failure, environmental impacts and remediation. Appl. Geochem. 51, 229–245.
Lambin, E.F., Ehrlich, D., 1996. The surface temperature–vegetation index space for land cover and land-cover change analysis. Int. J. Remote Sens. 17, 463–487.
Lin, Y.N., Simons, M., Hetland Eric, A., Muse, P., DiCaprio, C., 2010. A multiscale approach to estimating topographically correlated propagation delays in radar interferograms. Geochem. Geophys. Geosyst. 11, 1–17.
Martin, T.E., McRoberts, E.C., 1999. Some Considerations in the Stability Analysis of Upstream Tailing Dams. AGRA Earth & Environmental Limited, Canada.
Meckel, T.A., Ten Brink, U.S., Williams, S.J., 2007. Sediment compaction rates and subsidence in deltaic plains: numerical constraints and stratigraphic influences. Basin Res. 19, 19–31.
Morgenstern, N.R., Vick, S.G., Viotti, C.B., Watts, B.D., 2016. In: Samarco, S.A., Vale, S.A. (Eds.), Fundão Tailings Dam Review Panel: Report on the Immediate Causes of the Failure of the Fundão Dam. BHP Brasil Ltd., Mariana, Brazil. Available online: http://fundaoinvestigation.com/the-panel-report/ (Accessed 23 March 2019).
Mountrakis, G., Im, J., Ogole, C., 2011. Support vector machines in remote sensing: a review. ISPRS J. Photogramm. Remote Sens. 66, 247–259.
Nechad, B., Ruddick, K., Park, Y., 2010. Calibration and validation of a generic multisensor algorithm for mapping of total suspended matter in turbid waters. Remote Sens. Environ. 114, 854–866.

Ojha, C., Shirzaei, M., Werth, S., Argus, D.F., Farr, T.G., 2018. Sustained groundwater loss in California's Central Valley exacerbated by intense drought periods. Water Resour. Res. 54, 4449–4460.
Parida, B.R., Collado, W.B., Borah, R., Hazarika, M.K., Samarakoon, L., 2008. Detecting drought-prone areas of rice agriculture using a MODIS-derived soil moisture index. GISci. Remote Sens. 45, 109–129.
Porsani, J.L., Jesus, F.A.N., Stangari, M.C., 2019. GPR survey on an iron mining areas after the collapse of the Tailing Dam I at the Córrego do Feijão Mine in Brumadinho-MG, Brazil. Remote Sens. 11, 1–13.
Potić, I., Bugarski, M., Matić-Varenica, J., 2017. Soil moisture determination using remote sensing data for the property protection and increase of agriculture production. In: Responsible Land Governance: Towards an Evidence Based Approach 2017 World Bank Conference on Land and Poverty. The World Bank - Washington DC, March 20–24.
Riel, B., Simons, M., Ponti, D., Agram, P., Jolivet, R., 2018. Quantifying ground deformation in the Los Angeles and Santa Ana coastal basins due to groundwater withdrawal. Water Resour. Res. 54, 3557–3582.
Riley, S.J., DeGloria, S.D., Elliot, R., 1999. A terrain ruggedness index that quantifies topographic heterogeneity. Intermount. J. Sci. 5, 1–4.
Robertson, P.K., Melo, L., Williams, D.J., Wilson, G.W., 2020. Report of the Expert Panel on the Technical Causes of the Failure of Feijão Dam I. . Available at < https://bdrb1investigationstacc.z15.web.core.windows.net/assets/Feijao-Dam-I-Expert-Panel-Report-ENG.pdf > . (Accessed 24 March 2020).
Santamarina, J.C., Torres-Cruz, L.A., Barchus, R.C., 2019. Why coal ash and tailings dam disasters occur. Science 364, 526–528.
Sato, Y., Godinho, H.P., 2003. Migratory fishes of the São Francisco River. In: Carolsfeld, J., Harvey, B., Ross, C., Baer, A. (Eds.), Migratory Fishes of South America. World Fisheries Trust/The World Bank/International Development Research Centre, Ottawa, pp. 195–232.
Smith, M., 2002. Liquefaction in Dump Leaching. Mining Magazine.
Souza Jr., P.A., 2019. Open data could have helped us learn from another mining dam disaster. Sci. Data 6, 1–2.
Sun, Q., Jiang, L., Jiang, M., Lin, H., Ma, P., Wang, H., 2018. Monitoring coastal reclamation subsidence in Hong Kong with distributed scatterer interferometry. Remote Sens. 10, 1–23.
Thompson, F., et al., 2020. Severe impacts of the Brumadinho dam failure (Minas Gerais, Brazil) on the water quality of the Paraopeba River. Sci. Total Environ. 705, 135914.
Toming, K., Kutser, T., Laas, A., Sepp, M., Margot, S., Nõges, T., 2016. First experiences in mapping lake water quality parameters with Sentinel-2 MSI imagery. Remote Sens. 8, 1–14.
Zhan, Z., Qin, Q., Wang, X., 2004. The application of LST/NDVI index for monitoring land surface moisture in semiarid area. IGARSS 2004 - IEEE International Geoscience and Remote Sensing Symposium.